

On the tensile behaviors of 2D twill woven SiO_{2f}/SiO₂ composites at ambient and elevated temperatures: Mesoscale analysis and in situ experimental investigation

Duoqi Shi^{a,b}, Changqi Liu^a, Zhen Cheng^a, Zhenlei Li^{a,*}, Xiaoguang Yang^{a,b}, Haofeng Chen^c

^a School of Energy and Power Engineering, Beihang University, Beijing, 100191, China

^b Collaborative Innovation Center for Advanced Aero-Engine, Beijing, 100191, China

^c Department of Mechanical and Aerospace Engineering, University of Strathclyde, Glasgow, G1 1XJ, UK

ARTICLE INFO

Keywords:

SiO_{2f}/SiO₂

Twill woven composites

Digital image correlation

Progressive failure analysis

ABSTRACT

SiO_{2f}/SiO₂ composites are among the most ideal high-temperature wave-transparent materials used in hypersonic vehicles. The purpose of the study is the thorough experimental investigation of the tensile behavior of a 2D twill woven SiO_{2f}/SiO₂ composite, and the establishment of an accurate and efficient simulation method for such composites. The digital image correlation (DIC) method was utilized to capture local deformation data during tensile tests. Meanwhile, a progressive failure analysis (PFA) model employing the exponential damage evolution law was subsequently developed with UMAT in ABAQUS. Simulations of the mechanical properties and strain distributions show good consistency with experimental results. The results at room temperature and 900 °C demonstrate that the strain distributions exhibit obvious periodic patterns related to the woven structure. In addition, band-shaped strain concentrations can be observed at the intersection zones between adjacent longitudinal and transverse fiber bundles. These zones are regarded as critical regions. This was validated by the damage evolution observed in the simulations. Owing to the grain coarsening of quartz fibers and the embrittlement of different constituents at 900 °C, notable degradation of the mechanical properties and brittle fracture characteristics were observed.

1. Introduction

With the development of aerospace technologies, an increasing number of advanced ceramic matrix composites (CMCs) have attracted worldwide attention [1]. Quartz fibers reinforced silica matrix (SiO_{2f}/SiO₂) composites combine excellent dielectric properties, thermal shock damage resistance, low thermal conductivity, and acceptable mechanical properties. The unique integration of these properties exceeds the requirements for high-temperature wave-transparent materials intended for use in the radomes and antenna windows of hypersonic vehicles [2, 3]. Recently, various SiO_{2f}/SiO₂ composites have been fabricated, and their preparation parameters (such as heat treatment temperature) were investigated, including unidirectional [4], 2D woven [5], 2.5D woven [6–8], 3D orthogonal [3], 3D four-directional and 3D five-directional composites [9–11]. These studies have mainly focused on the dielectric, thermophysical, and room-temperature flexural properties of the composites. The flexural properties of SiO_{2f}/SiO₂ composites degrade

with increasing temperature, especially above 900 °C [12,13], which is related to the crystallization of quartz fibers at high temperatures [14]. Investigations of the tensile behaviors of SiO_{2f}/SiO₂ composites, at room temperature and typical operating temperatures, are limited.

When conducting mechanical tests of woven composites, the local deformation at the mesoscale must be analyzed to contribute to a deep understanding of damage initiation and propagation among different constituents. Digital image correlation (DIC) is a non-contact optical technique used to acquire in situ information relating to the surface displacement and strain fields. It has been proven to be a suitable technique for measuring the local deformation of metals [15]. In addition, it is well suited for measuring pre-cracking strain distributions and post-cracking damage evolution in woven CMCs [16]. In Ref. [16], DIC was utilized to reveal the effect of fiber architecture on strain concentrations and to study the initiation and propagation of cracks in 2D woven SiC_f/SiC composites. The damage development of a 2D braided SiC_f/SiC tube was investigated at the tow scale under tensile loading

* Corresponding author.

E-mail address: lizhl@buaa.edu.cn (Z. Li).

Table 1

The pristine properties of quartz fibers and silica matrix.

Quartz fiber		
Elastic modulus (GPa)	Poisson's ratio	Tensile strength (MPa)
72–78	0.25	1046
Silica matrix		
Elastic modulus (GPa)	Poisson's ratio	Tensile strength (MPa)
35–45	0.25	180–220

[17]. The deformation behavior and failure mechanism under the tensile loading of 2D and 2.5D woven $\text{SiO}_2/\text{SiO}_2$ composites were examined using the stereo-DIC technique at room temperature in Ref. [18]. Additionally, non-uniform strains in a 2.5D woven $\text{SiO}_2/\text{SiO}_2$ composite under in-plane tensile stress were observed and quantitatively analyzed in Ref. [19]. DIC has also been applied to study the tensile behaviors of notched SiC_f/SiC and $\text{Al}_2\text{O}_3/\text{Al}_2\text{O}_3\text{-SiO}_2$ composites [20,21].

Because of the dispersion of the properties of textile composites and the high costs of experiments, mesoscale numerical simulation is considered as a reliable, precise and efficient method to predict the macroscopic mechanical properties and reproduce the damage evolution of woven or braided CMCs [22]. A mesoscale geometric model of textile composites can be generated in computer-aided design (CAD) software based on the geometric parameters from micro-computational tomography (CT) [23] or microscope images [19]. For composites with relatively simple woven structure, such as 2D twill woven composites, geometric model can be established directly in open-source textile modelers, such as TexGen [24] and WiseTex [25]. After determining the

properties of the different constituents and establishing the mesoscale geometric model, the elastic properties can be subsequently calculated in commercial finite-element software, for example, ABAQUS. The in-plane elastic properties of 2D twill woven T300 carbon/epoxy composites were acquired by experimental and numerical methods in Ref. [26].

In addition to calculating the elastic properties of composites, it is also necessary to predict the damage evolution behavior and strength in numerical simulations. For decades, progressive failure analysis (PFA) has been applied to mesoscale simulations of textile composites [27]. In a PFA model, the damage initiation criteria and damage evolution laws are the two most important aspects. A 2D progressive damage model was developed for elastic–brittle fiber-reinforced materials in Ref. [28], Hashin criteria and damage variables defined by equivalent displacements were used to identify the initial damage and degradation of the material properties, respectively. This model was embedded into ABAQUS. A similar PFA was conducted to study the mechanical behaviors of a 2D twill woven T300 carbon/epoxy composite in Ref. [29]. In Ref. [30], exponential damage evolution laws (proposed in Ref. [31]) were used to gradually degrade the material properties of a 2.5D woven $\text{SiO}_2/\text{SiO}_2$ composite.

This paper aims to investigate the tensile behaviors of a 2D twill woven $\text{SiO}_2/\text{SiO}_2$ composites by experiments, and to establish an effective and efficient simulation method for engineering applications. First, DIC was used to provide in-situ full-field information during the tests. Numerical simulations were used to study the gauge section of composites at mesoscale and a PFA model was subsequently

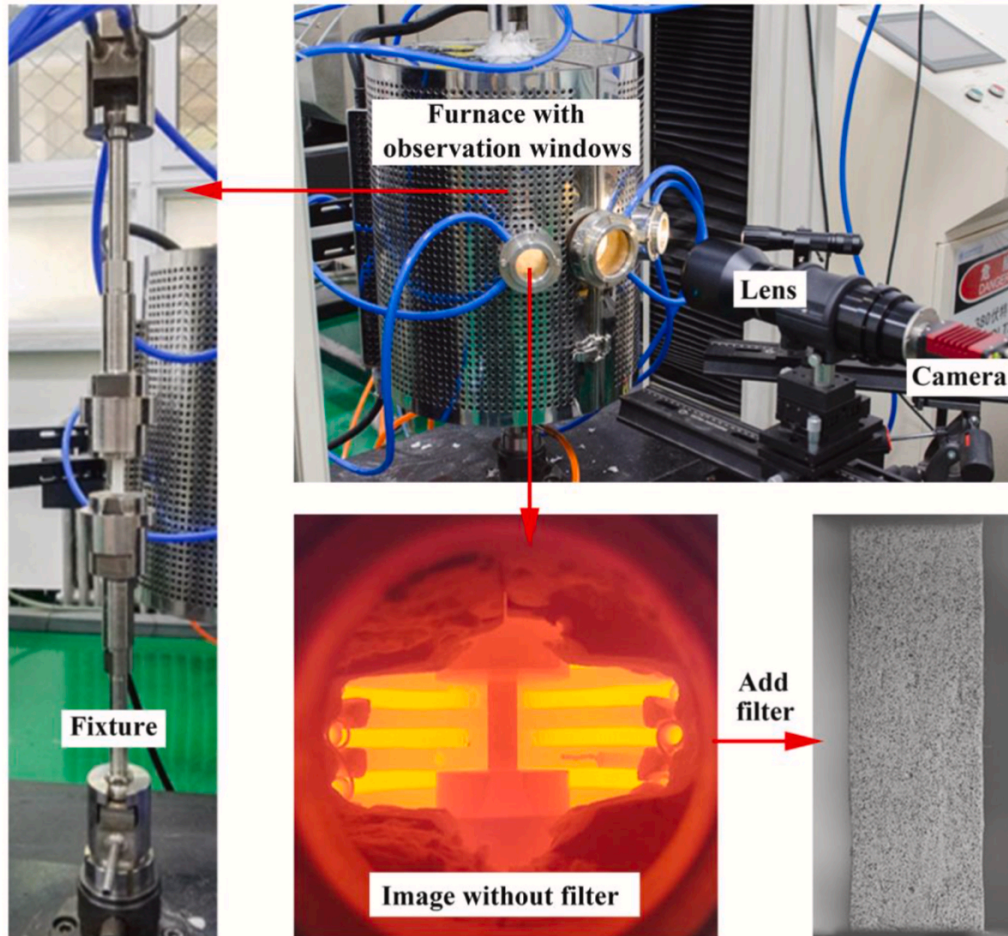


Fig. 1. Complete experimental system used to perform tensile tests with DIC at 900 °C.

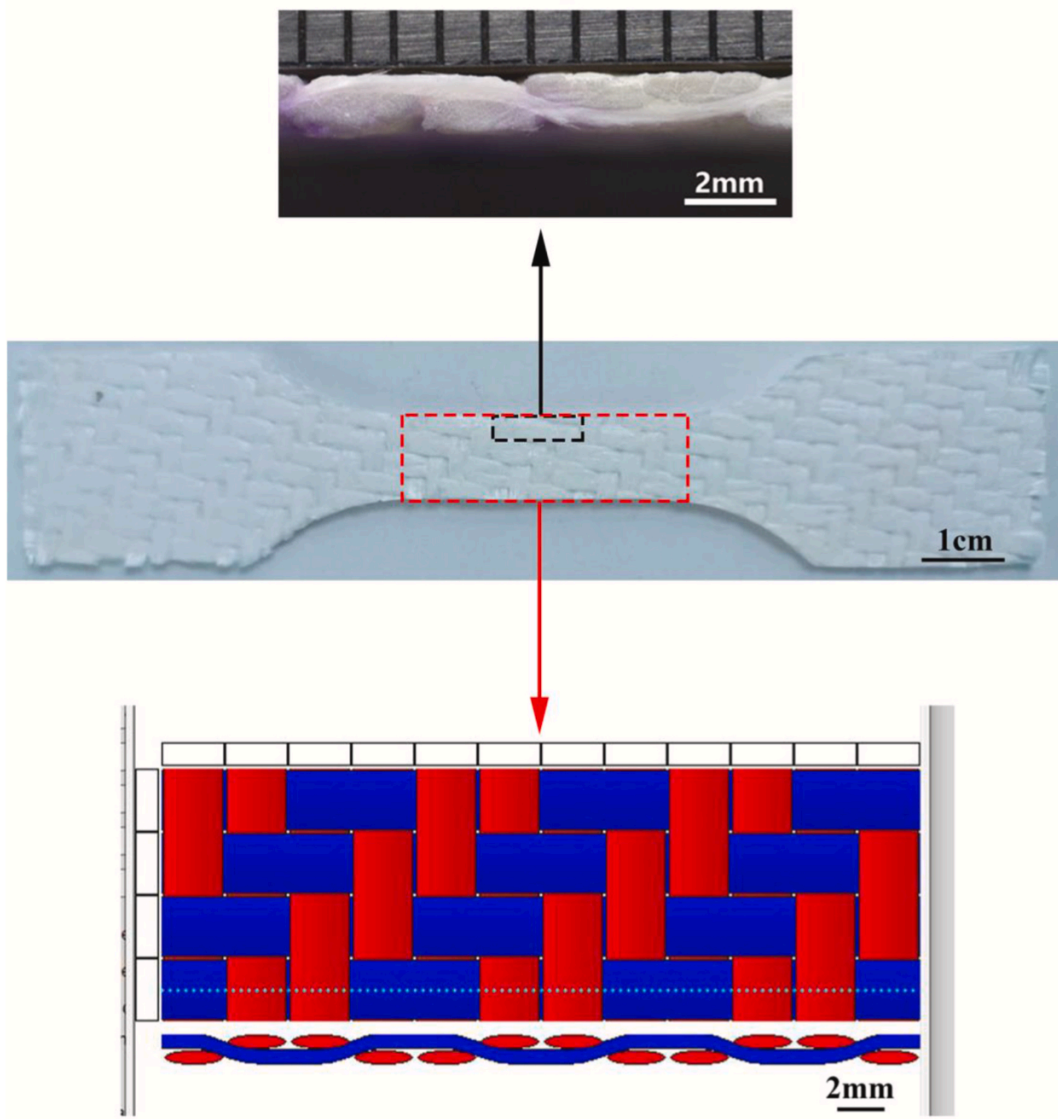


Fig. 2. Pictures of one tested specimen and corresponding schematic given in TexGen.

implemented via UMAT in ABAQUS. Strain fields and damage evolution were well reproduced in the simulations. Finally, the deformation characteristics, critical regions, and failure mechanisms of the 2D twill woven $\text{SiO}_{2f}/\text{SiO}_2$ composites under tensile loading at room temperature and 900 °C were comprehensively discussed through the combined analysis of the in-situ experiments and finite-element simulations.

2. Tensile tests with DIC

The quartz fibers used in the 2D twill woven $\text{SiO}_{2f}/\text{SiO}_2$ composites were provided by Feilihua Quartz Glass Corp., China, with diameters of 6–10 μm . The fibers were woven into a 2D fabric preform, followed by heat treatment and infiltration of the silica sol. The products were sintered at 800 °C. The infiltration–sintering processes were repeated four times to acquire the composites. This fabrication route is called the sol-gel method [11,32,33]. The fiber volume fraction and density of the prepared $\text{SiO}_{2f}/\text{SiO}_2$ composites were 45% and 1.6 g/cm^3 , respectively. The pristine properties of the quartz fibers and silica matrix are presented in Table 1 [30]. However, the properties of different constituents are degraded when sintered at high temperatures during preparation. Moreover, the matrix in the as-fabricated composites is porous. Eq. (1) is

usually used to degrade the stiffness and strength of the porous matrix [34]:

$$S = S_0 \cdot e^{-\omega f} \quad (1)$$

where S is the stiffness or strength of the porous matrix, and S_0 is the stiffness or strength of the pure matrix. f represents the matrix porosity, and ω is an empirical constant.

These issues can cause conspicuous degradations in the properties of various constituents in the as-fabricated composites. The specimens used in the present work were cut from a large $\text{SiO}_{2f}/\text{SiO}_2$ composite sheet and then machined into a dog-bone shape. Their overall size was $120 \times 25 \times 1.5$ (length \times width \times thickness, mm) with a gauge section of approximately $30 \times 10 \times 1.2$ mm.

Tensile tests were conducted on a 5-kN-capacity WDW-100 universal testing machine (Changchun Research Institute of Testing Machines, Jilin, China) at room temperature and a typical operating temperature (900 °C). The specimens were placed in a fixture with a self-adjusting alignment function and then loaded with a crosshead displacement speed of 0.4 mm/min. A furnace with observation windows was used for testing when the specimens were tested at 900 °C. During the tests, a

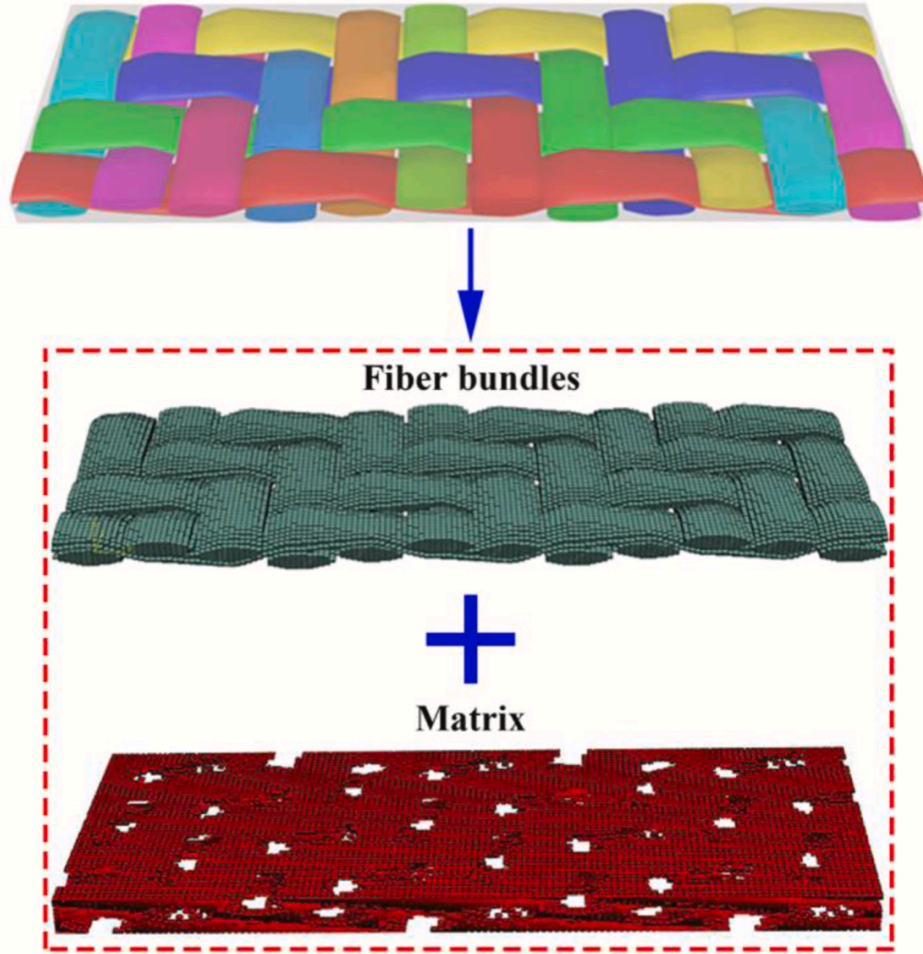


Fig. 3. Mesoscopic geometry and finite-element mesh of the gauge section of the composites.

charge-coupled device (CCD) camera with a double telecentric lens (magnification ratio, 1:5) recorded images at a frame rate of 15 fps, with a 17.25- μm pixel size. The entire experimental system used to perform tensile tests with DIC at 900 °C is shown in Fig. 1.

DIC analysis was conducted using the software VIC-2D (Correlated Solutions), with an image subset dimension of 29×29 pixels and a step size of 5 pixels. The strain fields were calculated from the full-field displacements using a centered three-point differentiation scheme.

3. Mesoscale finite element model

3.1. Geometric model

Before constructing the geometric model, mesoscale pictures were taken to obtain the woven pattern and geometric parameters of the composites. The mesoscale structure of the gauge section of the composites was then recreated in Texgen. A general 2D woven pattern was embedded in the software; the crossing of the fiber bundles required manual adjustment. Afterwards, the size of the gauge section was defined as 10.1 mm \times 1.2 mm \times 30 mm. Other parameters such as the height of the fiber bundles (0.5 mm), the width of the fiber bundles (2.4

Table 2

The parameters used in the simulations at room temperature.

Fiber bundles								
$E_{f,LL}$ (GPa)	$E_{f,TT}$ (GPa)	$E_{f,ZZ}$ (GPa)	$G_{f,LT}$ (GPa)	$G_{f,LZ}$ (GPa)	$G_{f,TZ}$ (GPa)	$\mu_{f,LT}$	$\mu_{f,LZ}$	$\mu_{f,TZ}$
11	3	3	1.8	1.2	1.2	0.26	0.26	0.26
$S_{f,LL}$ (MPa)	$S_{f,TT}$ (MPa)	$S_{f,ZZ}$ (MPa)	$S_{f,LT}$ (MPa)	$S_{f,TT}$ (MPa)	$S_{f,ZZ}$ (MPa)	$S_{f,LT}$ (MPa)	$S_{f,TT}$ (MPa)	$S_{f,LT}$ (MPa)
80	50	60	40	60	40	25	25	25
$G_{ff,LL}$ (J/m ²)	$G_{ff,TT}$ (J/m ²)	$G_{ff,ZZ}$ (J/m ²)	η					
0.8	0.8	0.8	0.005					
Silica matrix								
E_m (GPa)	G_m (GPa)	μ_m	$S_{m,t}$ (MPa)	$S_{m,c}$ (MPa)	G_{fm} (J/m ²)	η		
2.1	1	0.35	15	15	0.1	0.005		

Table 3

The parameters used in the simulations at 900 °C.

Fiber bundles								
$E_{f,L}$ (GPa)	$E_{f,T}$ (GPa)	$E_{f,Z}$ (GPa)	$G_{f,LT}$ (GPa)	$G_{f,LZ}$ (GPa)	$G_{f,TZ}$ (GPa)	$\mu_{f,LT}$	$\mu_{f,LZ}$	$\mu_{f,TZ}$
10	2.5	2.5	1.5	1	1	0.26	0.26	0.26
$S_{f,Lt}$ (MPa)	$S_{f,Tt}$ (MPa)	$S_{f,Zt}$ (MPa)	$S_{f,Lc}$ (MPa)	$S_{f,Tc}$ (MPa)	$S_{f,Zc}$ (MPa)	$S_{f,LT}$ (MPa)	$S_{f,LT}$ (MPa)	$S_{f,LT}$ (MPa)
60	35	45	30	45	30	20	20	20
$G_{ff,L}$ (J/m ²)	$G_{ff,T}$ (J/m ²)	$G_{ff,Z}$ (J/m ²)	η					
0.6	0.6	0.6	0.005					
Silica matrix								
E_m (GPa)	G_m (GPa)	μ_m	$S_{m,t}$ (MPa)	$S_{m,c}$ (MPa)	G_{fm} (J/m ²)	η		
1.7	0.8	0.35	12	12	0.1	0.005		

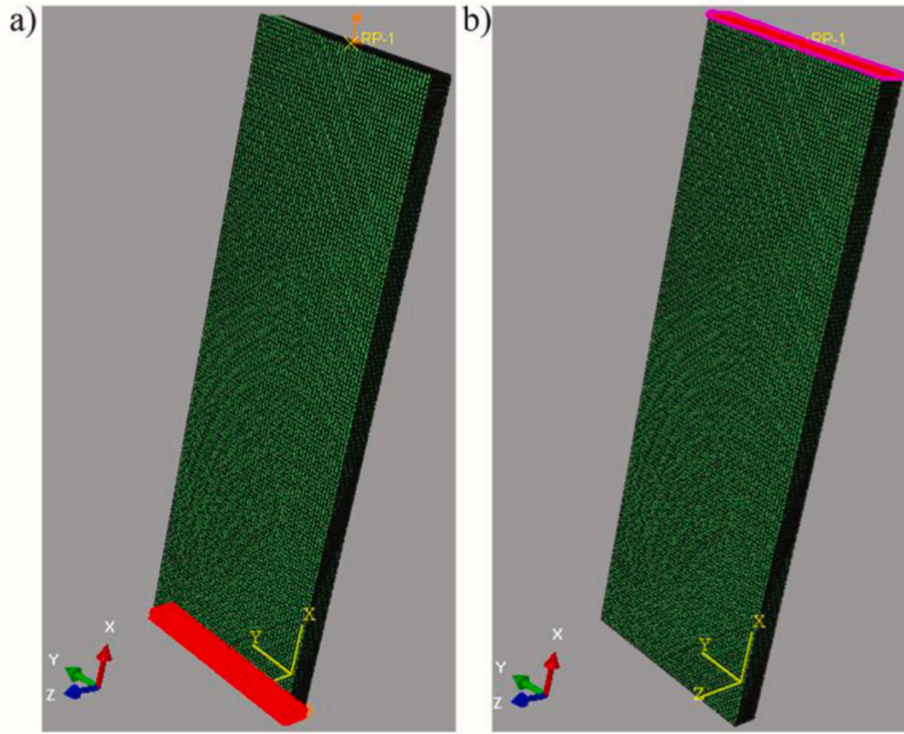
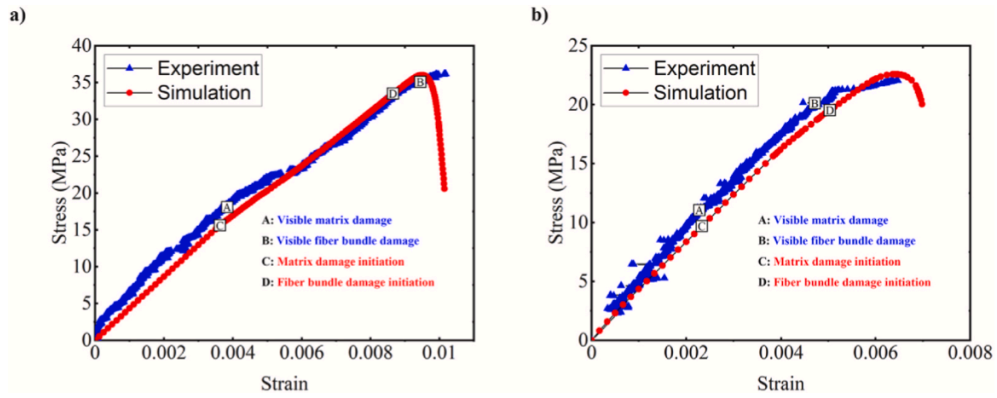
**Fig. 4.** a) The boundary conditions and b) loading mode used in the finite-element simulations.**Fig. 5.** The experimental and simulated stress–strain curves at a) room temperature and b) 900 °C.

Table 4

The comparison of experimental and simulated values of the elastic moduli and ultimate strengths at various temperatures.

Room temperature		
Elastic modulus (GPa)	Experimental results	Simulated results
Ultimate strength (MPa)	36.16	36.02
900°C		
Elastic modulus (GPa)	Experimental results	Simulated results
Ultimate strength (MPa)	22.04	22.58

mm), and the central distance between two adjacent fiber bundles (2.5 mm) were also defined to obtain the final model. The local coordinate systems were assigned to the fiber bundles in the software TexGen. The material properties of the fiber bundles were then applied according to the local coordinate systems. Pictures of one tested specimen and the corresponding schematic are shown in Fig. 2. Finite-element meshes of different constituents were also generated in TexGen. Hexahedral elements (C3D8) were used to improve the efficiency and accuracy of the finite-element calculation. Fig. 3 depicts the mesoscopic geometry and finite-element mesh of the gauge sections of the composites.

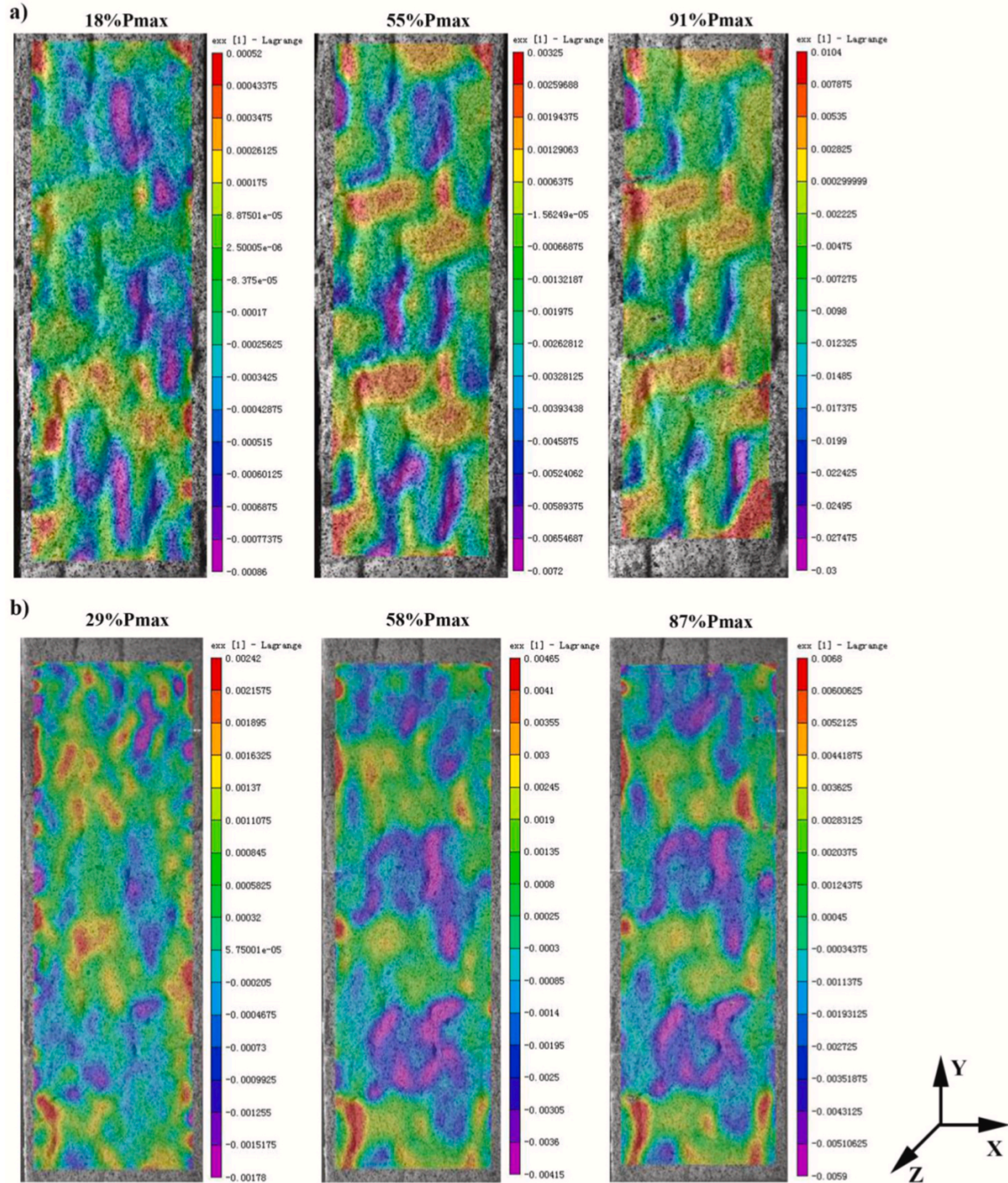


Fig. 6. The evolution of the transverse strains ϵ_{xx} with increasing load at a) at room temperature and b) 900 °C.

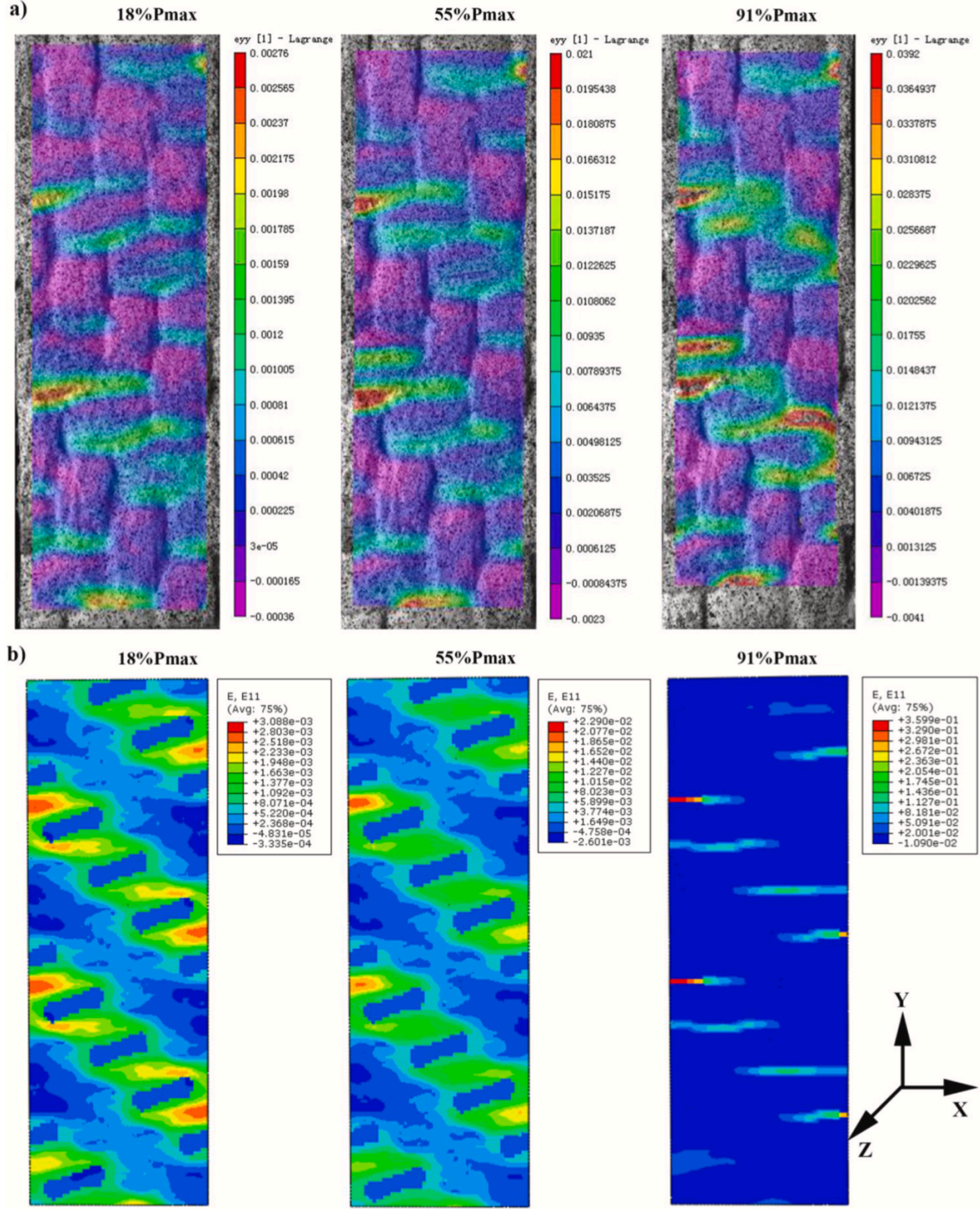


Fig. 7. a) The evolution of the longitudinal strains ϵ_{yy} with increasing load at room temperature and b) corresponding simulation results.

3.2. Damage initiation criteria

The matrix was considered as an isotropic material and the maximum stress criterion was applied to identify the initial damage of the matrix. The fiber bundles were modeled as unidirectional composites with transversely isotropic properties. Hashin's failure criterion, which considers the tensile and compressive damage of different constituents, has been widely used for predicting the failure of unidirectional fiber composites [35]. Therefore, the 3D Hashin criterion was adopted for the fiber bundles. The 3D Hashin criterion including four

distinct failure modes, is presented below:

Tensile Fiber Mode $\sigma_{11} > 0$,

$$F_{f,Lt} = \frac{\sigma_{11}^2}{S_{f,Lt}^2} + \frac{(\tau_{12}^2 + \tau_{13}^2)}{S_{f,Lt}^2} = 1 \quad (2)$$

Compressive Fiber Mode $\sigma_{11} < 0$,

$$F_{f,Lc} = -\frac{\sigma_{11}}{S_{f,Lc}} = 1 \quad (3)$$

Tensile Matrix Mode $\sigma_{22} + \sigma_{33} > 0$,

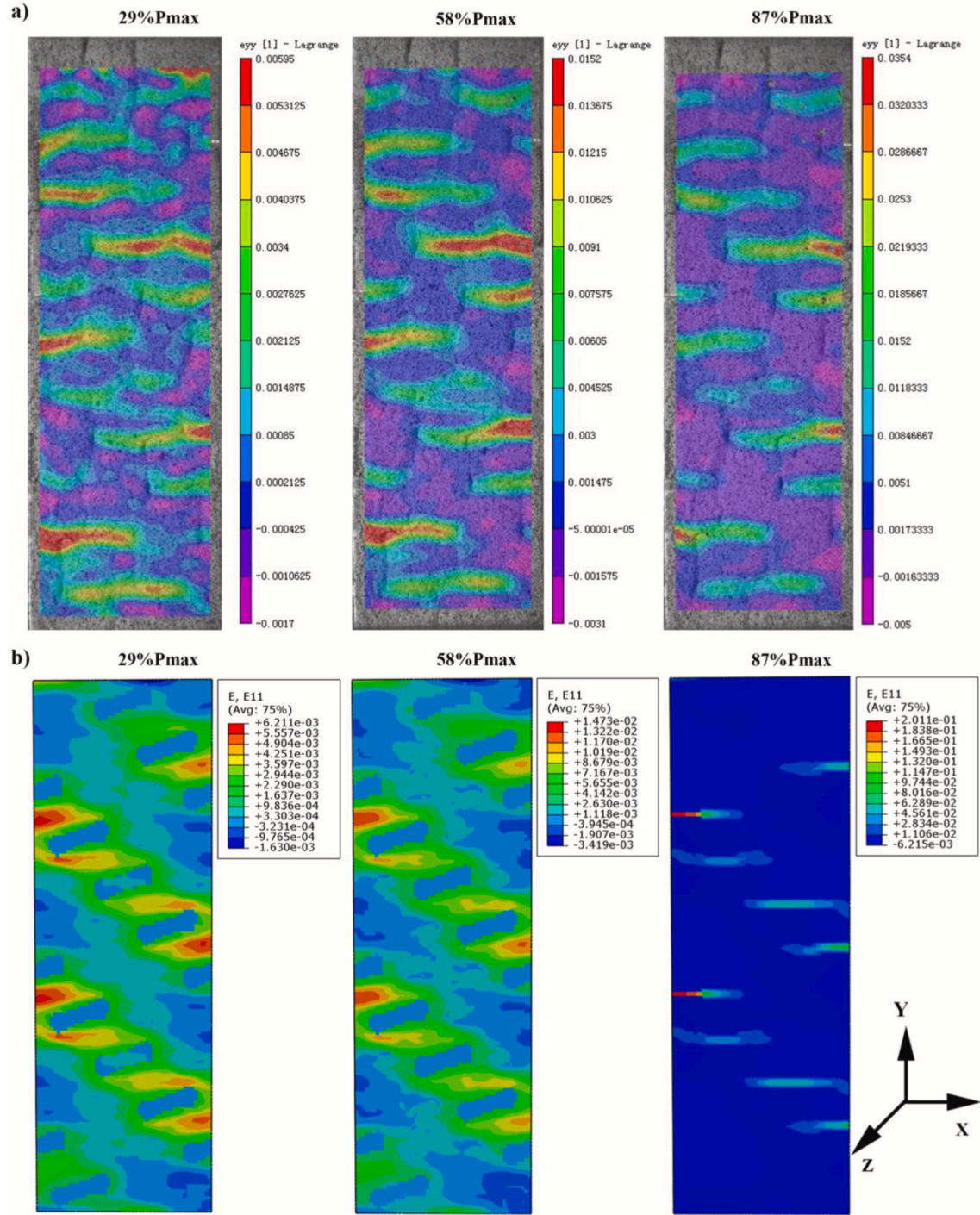


Fig. 8. a) The evolution of the longitudinal strains ϵ_{yy} with increasing load at 900 °C and b) corresponding simulation results.

$$F_{f,Tt} = \frac{(\sigma_{22} + \sigma_{33})^2}{S_{f,Tt}^2} + \frac{(\tau_{23}^2 - \sigma_{22}\sigma_{33})}{S_{f,TZ}^2} + \frac{(\tau_{12}^2 + \tau_{13}^2)}{S_{f,LT}^2} = 1 \quad (4)$$

Compressive Matrix Mode $\sigma_{22} + \sigma_{33} < 0$,

$$F_{f,Tc} = \frac{1}{S_{f,Tc}^2} \left[\left(\frac{S_{f,Tc}}{2S_{f,TZ}} \right)^2 - 1 \right] (\sigma_{22} + \sigma_{33})$$

$$+ \frac{(\sigma_{22} + \sigma_{33})^2}{4S_{f,TZ}^2} + \frac{(\tau_{23}^2 - \sigma_{22}\sigma_{33})}{S_{f,TZ}^2} + \frac{(\tau_{12}^2 + \tau_{13}^2)}{S_{f,LT}^2} = 1 \quad (5)$$

where σ and τ are the applied stresses, and T , C , and S are the tensile, compressive, and shear strengths, respectively.

3.3. Damage evolution model

When the stress state of one element satisfies the damage initiation criteria as given in Section 3.2, the material properties degrade gradually according to the damage evolution law, that relates the mesoscale damage to micromechanical failure mechanisms. Teng et al. [30] proposed a continuum damage model to conduct a PFA of a 2.5D woven

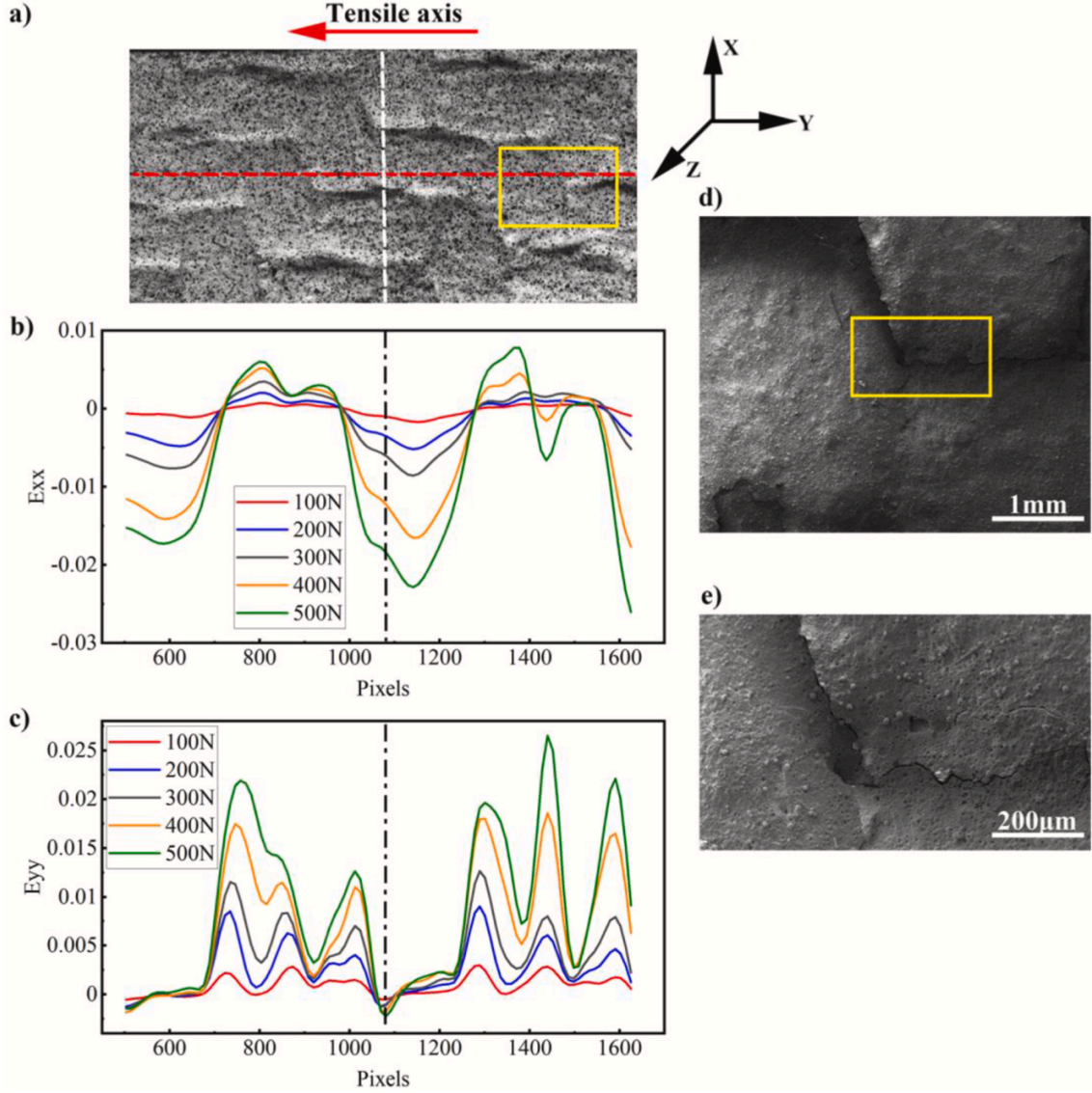


Fig. 9. Profiles of local strains measured by DIC at room temperature for two woven RVEs: a) two RVEs of the composite; b) transverse and c) longitudinal strain distributions along the red line in a); d) the SEM image of the yellow rectangular region in a); e) the SEM image of the yellow rectangle region in d). (For interpretation of the references to color in this figure legend, the reader is referred to the Web version of this article.)

SiO₂f/SiO₂ composite, in which two damage variables $d_{f,L}$ and $d_{f,T}$ with similar forms were used to model the degradation in the stiffness of fiber bundles. For fiber bundles, the exponential damage evolution law is given as follows:

$$d_{f,L} = \begin{cases} 1 - \frac{1}{F_{f,Lt}} \exp\left[(1 - F_{f,Lt})LS_{f,Lt}^2/E_{f,L}G_{Ff,L}\right] & \sigma_{11} > 0 \\ 1 - \frac{1}{F_{f,Lc}} \exp\left[(1 - F_{f,Lc})LS_{f,Lc}^2/E_{f,L}G_{Ff,L}\right] & \sigma_{11} < 0 \end{cases} \quad (6)$$

$$d_{f,T} = \begin{cases} 1 - \frac{1}{F_{f,Tt}} \exp\left[(1 - F_{f,Tt})LS_{f,Tt}^2/E_{f,T}G_{Ff,T}\right] & \sigma_{22} + \sigma_{33} > 0 \\ 1 - \frac{1}{F_{f,Tc}} \exp\left[(1 - F_{f,Tc})LS_{f,Tc}^2/E_{f,T}G_{Ff,T}\right] & \sigma_{22} + \sigma_{33} < 0 \end{cases} \quad (7)$$

where F is the damage threshold in the above damage initiation criteria. L is the characteristic element length; S , E and G_F are the strength, elastic modulus and fracture energy of different constituents respectively; the

subscripts Lt , Lc , Tt and Tc represent the material properties in various directions under either tension (t) or compression (c). For the matrix, the form of the damage evolution model is similar to Eqs. (6) and (7):

During the damage evolution process, the effective stiffness matrix is reduced by the damage variables. For the fiber bundles, the damaged stiffness matrix can be written as:

$$C_d = \begin{bmatrix} b_1 C_{11} & b_1 b_2 C_{12} & b_1 b_2 C_{13} & 0 & 0 & 0 \\ b_1 b_2 C_{12} & b_2 C_{22} & b_2 C_{23} & 0 & 0 & 0 \\ b_1 b_2 C_{13} & b_2 C_{23} & b_2 C_{33} & 0 & 0 & 0 \\ 0 & 0 & 0 & b_1 b_2 C_{44} & 0 & 0 \\ 0 & 0 & 0 & 0 & b_1 b_2 C_{55} & 0 \\ 0 & 0 & 0 & 0 & 0 & b_2 C_{66} \end{bmatrix} \quad (8)$$

where $b_1 = 1 - d_{f,L}$, $b_2 = 1 - d_{f,T}$.

To improve the convergence of the calculations, viscous damage variables are introduced:

$$\dot{d}_{f,L}^v = \frac{1}{\eta} (d_{f,L} - d_{f,L}^v) \quad (9)$$

$$\dot{d}_{f,T}^v = \frac{1}{\eta} (d_{f,T} - d_{f,T}^v) \quad (10)$$

here, $d_{f,L}^v$ and $d_{f,T}^v$ are regularized damage variables corresponding to $d_{f,L}$ and $d_{f,T}$ respectively, they are used in the calculations of the damaged stiffness matrix and the Jacobian matrix. η is the viscosity parameter controlling the rate at which the regularized damage variables $d_{f,L}^v$ and $d_{f,T}^v$ approach the true damage variables $d_{f,L}$ and $d_{f,T}$.

The relationship between stress and strain can be described as:

$$\sigma = C_d : \varepsilon \quad (11)$$

By differentiating the above equation, the Jacobian matrix can be formulated as:

$$\frac{\partial \Delta \sigma}{\partial \Delta \varepsilon} = C_d + \left[\left(\frac{\partial C_d}{\partial d_{f,L}^v} : \varepsilon \right) \left(\frac{\partial d_{f,L}}{\partial F_{f,L}} : \frac{\partial F_{f,L}}{\partial \varepsilon} \right) + \left(\frac{\partial C_d}{\partial d_{f,T}^v} : \varepsilon \right) \left(\frac{\partial d_{f,T}}{\partial F_{f,T}} : \frac{\partial F_{f,T}}{\partial \varepsilon} \right) \right] \frac{\Delta t}{\Delta t + \eta} \quad (12)$$

where $\Delta \sigma$ and $\Delta \varepsilon$ are the increments of stress and strain, respectively.

The parameters used in the simulations at room temperature and at 900 °C are summarized in Table 2 and Table 3 respectively.

3.4. Boundary condition and loading mode

Considering that the geometric model is the gauge section of the specimen, a simple displacement boundary condition is adopted in this study. Three-direction displacements of all nodes on the surface perpendicular to the X-axis are limited to zero, as shown in Fig. 4a. Because a displacement-controlled loading mode is used in the experiments, a similar loading mode is set in ABAQUS. More specifically, the

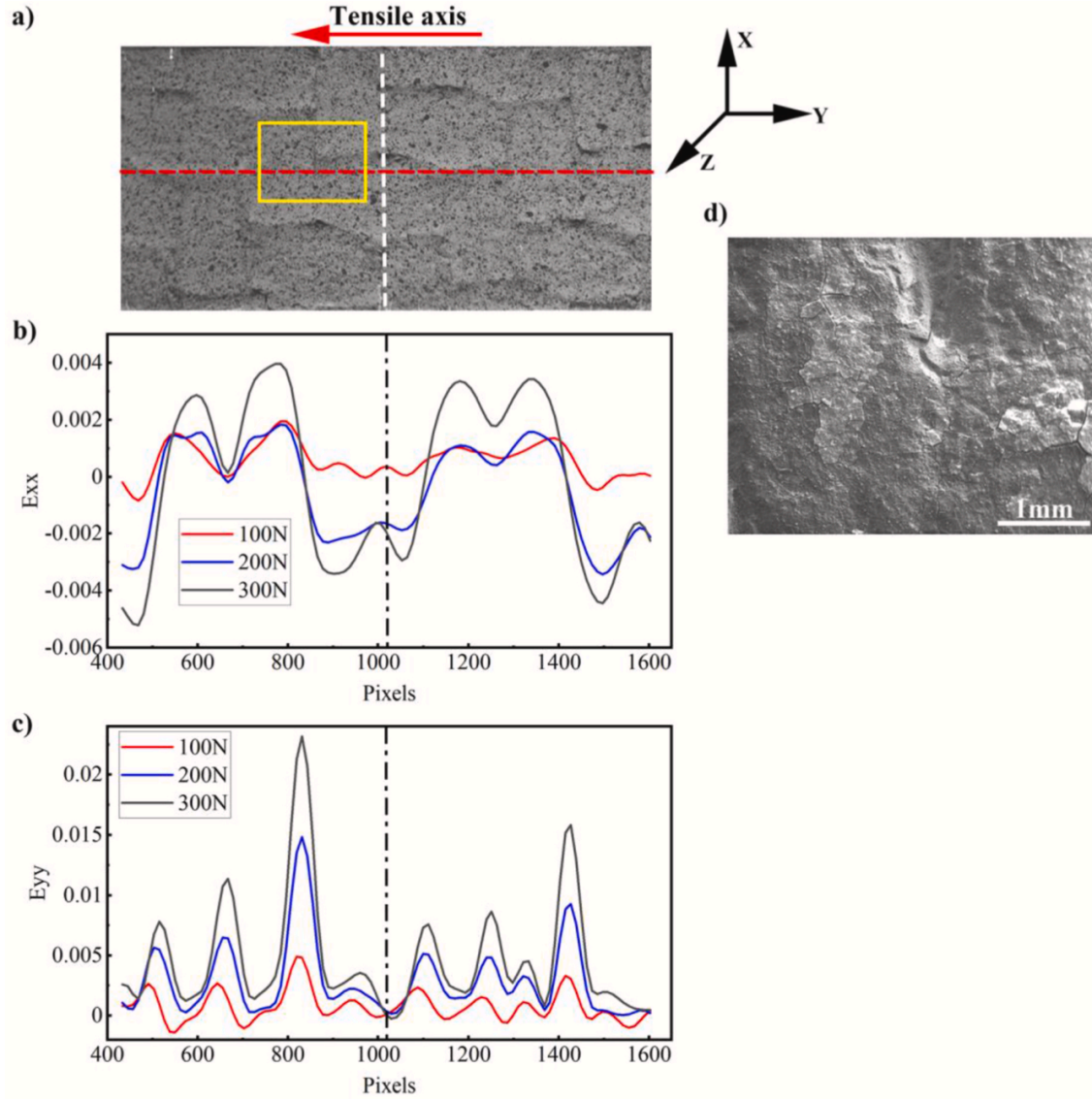


Fig. 10. Profiles of local strains measured by DIC at 900 °C for two woven RVEs: a) two RVEs of the composite; b) transverse and c) longitudinal strain distributions along the red line in a); d) the SEM image of the yellow rectangular region in a). (For interpretation of the references to color in this figure legend, the reader is referred to the Web version of this article.)

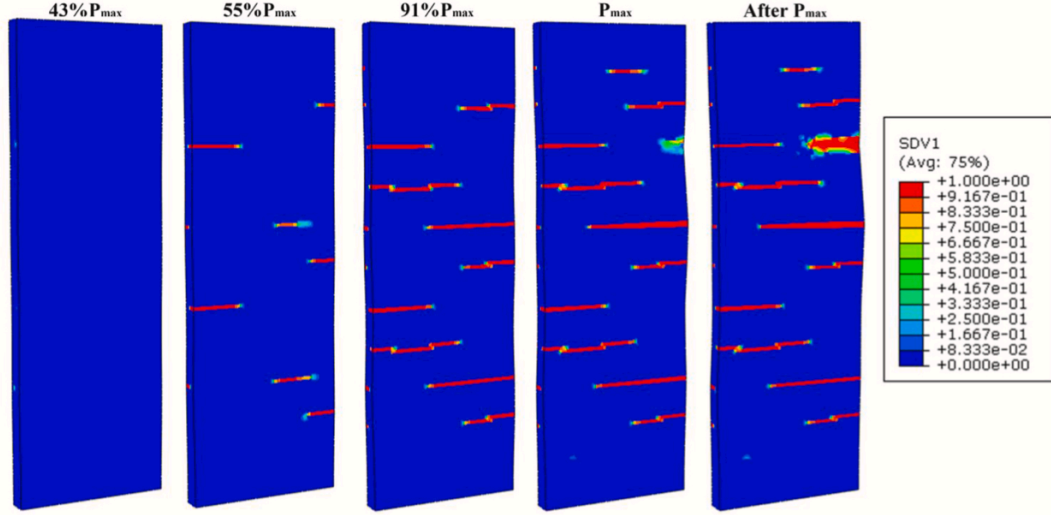


Fig. 11. Simulated damage evolution including that to both matrix and fiber bundles with increasing load at room temperature.

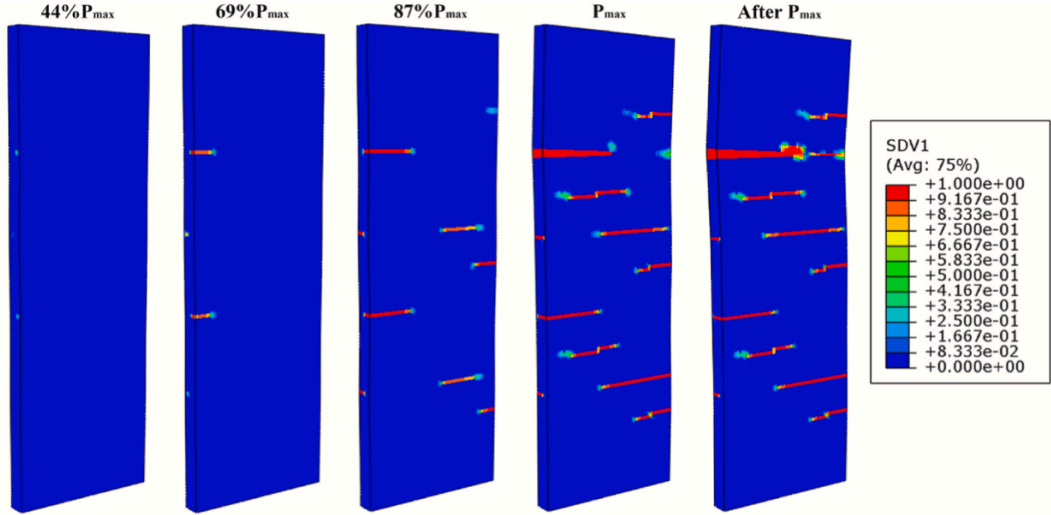


Fig. 12. Simulated damage evolution including that to both matrix and fiber bundles with increasing load at 900 °C.

three-direction displacements of all nodes on the other surface perpendicular to the X-axis are constrained by a reference point. The displacement is applied through reference point 1 (RP1 in Fig. 4b).

4. Results and discussion

4.1. Stress-strain curves

The experimental and simulated stress-strain curves at room temperature and 900 °C are shown in Fig. 5a and Fig. 5b, respectively. The strain data of the experimental curves were derived from the mean values of all points' longitudinal strains within three representative volume elements (RVEs) obtained from the DIC results. It can be seen that the predicted curves show good agreement with the experimental results. At room temperature, the longitudinal elastic modulus is approximately 4.36 GPa. The simulated modulus (4.31 GPa) agrees well with this experimental measurement. When the stress reaches 16.00 MPa (44% of the maximum stress), the curve begins to show nonlinearity, indicating the appearance of damage. In this stage, damage occurred by matrix cracking. The label "A" on the experimental stress-strain curve represents the visible matrix damage, and the

corresponding stress is 18.08 MPa (50% of the maximum stress). "C" on the predicted curve represents the initiation of matrix damage in the simulation, which coincides with the nonlinear stage. Fiber bundle damage occurs when the stress reaches 93% of its maximum value, indicated by "D" on the predicted curve. Visible fiber bundle damage is captured in the experiment until the stress reaches 35.07 MPa (97% of the maximum stress). The experimental and predicted values of ultimate strength are 36.16 MPa and 36.02 MPa, which show good agreement.

At 900 °C, owing to the degradation of the material properties of the quartz fibers and SiO₂ matrix, the longitudinal elastic modulus of the composite (4.05 GPa) is smaller than that at room temperature. This modulus degradation was also accurately captured by the simulation with a value of 4.09 GPa. As shown in Fig. 5, the stress-strain curve at 900 °C exhibits a different tendency compared to the curve at room temperature. The points "A", "B", "C" and "D" in Fig. 5b mark typical moments of damage evolution, which are the same as those in Fig. 5a. The curve increases almost linearly until the stress reaches 20.10 MPa ("B"), which reveals that initial matrix damage has little effect on the elastic modulus. Grain coarsening at 900 °C results in the strength degradation of the quartz fibers, leading to an earlier failure of the composite at high temperatures. This explains the decrease in the

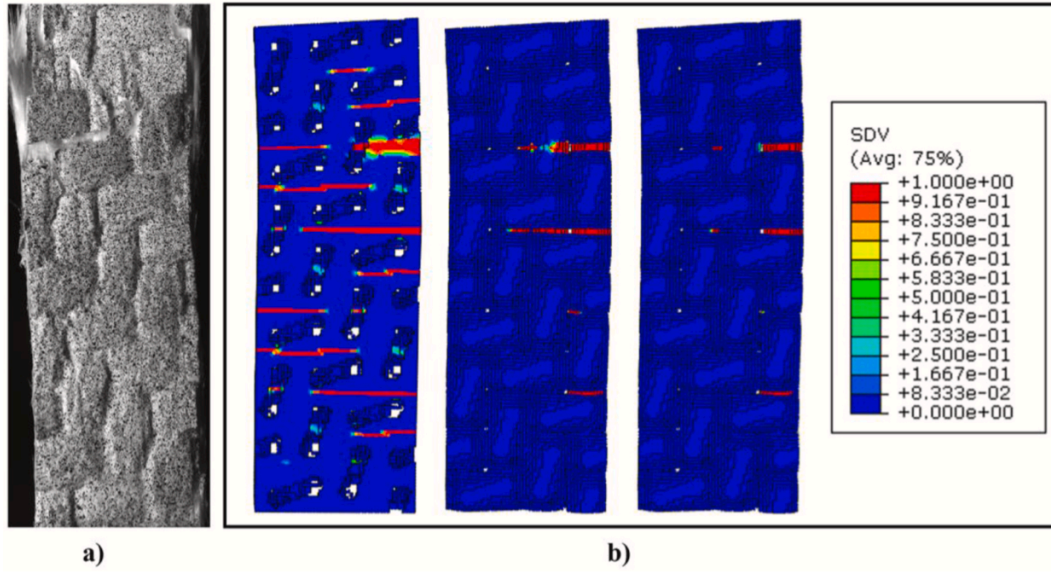


Fig. 13. The condition of final failure: a) captured during the experiments and b) simulated in the PFA at room temperature.

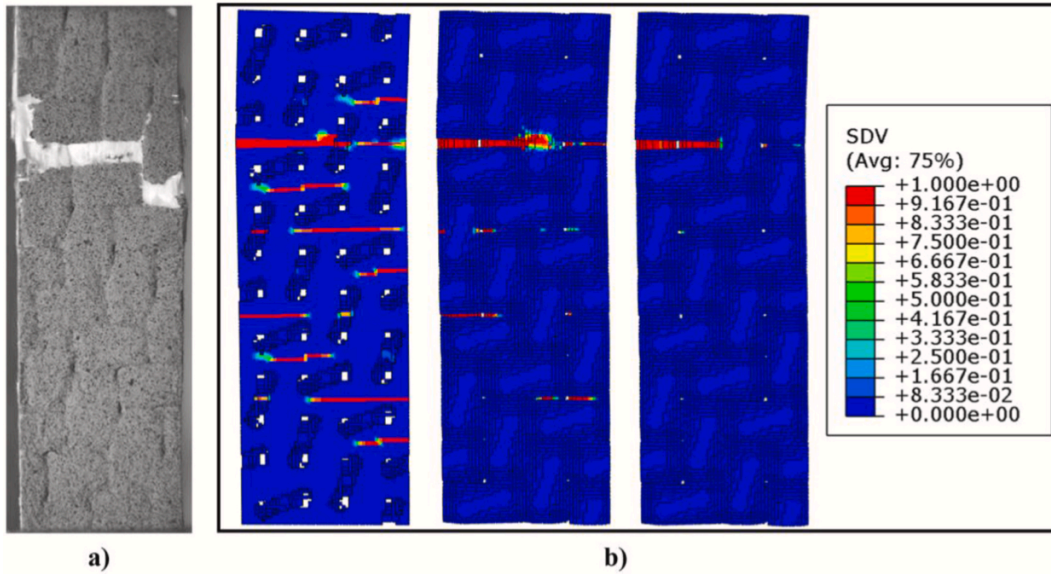


Fig. 14. The condition of final failure: a) captured during the experiments and b) simulated in the PFA at 900 °C.

ultimate strength (22.04 MPa), which was also accurately predicted by the simulation (22.58 MPa).

A comparison of the experimental and simulated results with respect to the elastic modulus and ultimate strength at various temperatures is shown in Table 4.

4.2. Strain distributions

Fig. 6 maps the evolution of the transverse strains ϵ_{xx} with increasing load at room temperature and 900 °C. The distribution of transverse strains ϵ_{xx} exhibits obvious periodic patterns as the stress increases to a certain level at room temperature. The strain fields are strongly related to the woven patterns of the composite. The transverse strains ϵ_{xx} at the regions of the longitudinal fiber bundles are negative. The porous matrix between longitudinal bundles has a higher level of negative strains because of its lower compressive modulus [1,9]. In contrast,

transverse fiber bundles exhibit positive strains, which are probably related to the interaction between adjacent fiber bundles as well as to the residual thermal stresses in the fiber bundles. The loads carried by the fiber bundles can be divided into external and internal loads. The interaction between adjacent bundles is a form of external load. The residual thermal stresses, as a kind of internal load, generally result from the mismatch between the thermal expansion coefficients of the fibers and the matrix. At 900 °C, the deformation behavior is similar to that at room temperature, but the strain fields show weaker periodic characteristics. Moreover, the strain levels at the surfaces of the longitudinal fiber bundles are much closer to that of the porous matrix between them. This phenomenon indicates that the severe degradation of the properties of the quartz fibers at high temperatures notably decreases the compressive modulus of the fiber bundles.

Fig. 7 shows the evolution of the longitudinal strains ϵ_{yy} with increasing load at room temperature and the corresponding simulation

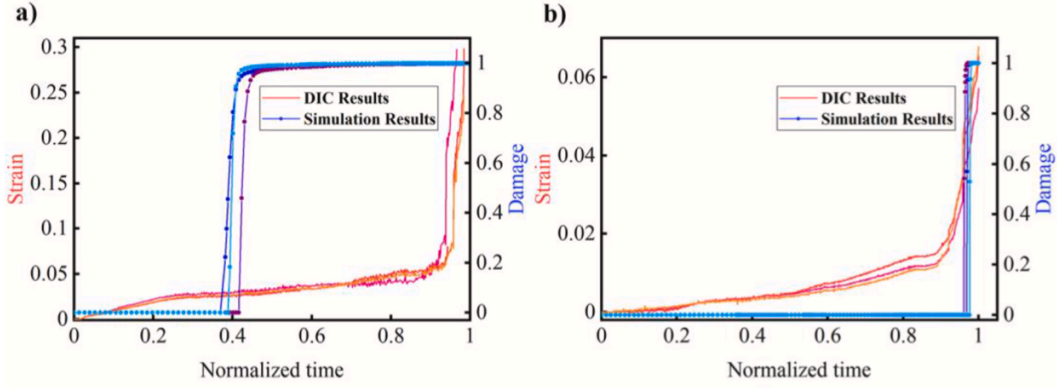


Fig. 15. The ε_{yy} evolution and damage development of individual points near the locations of final failure at room temperature: a) in the matrix region; b) in the fiber bundles region.

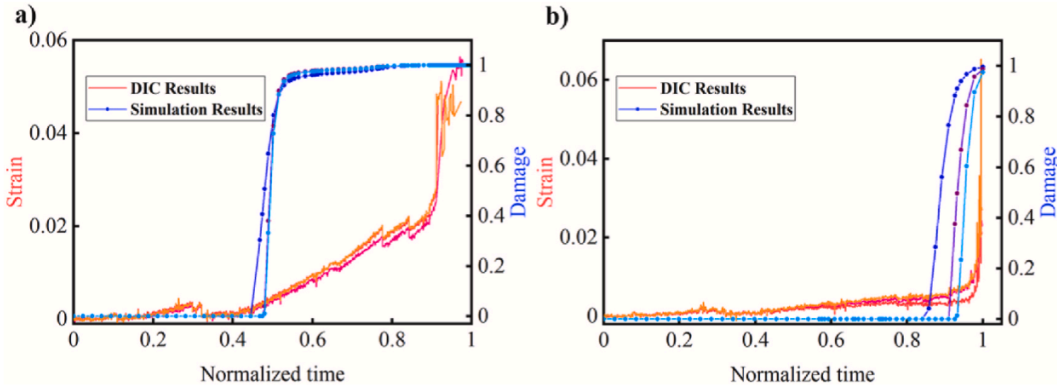


Fig. 16. The ε_{yy} evolution and damage development of individual points near the locations of the final failure at 900 °C: a) in the matrix region; b) in the fiber bundles region.

results. Similar to the transverse strain fields, the longitudinal strain distribution also correlated well with the woven structure. However, the distribution was more localized. In Fig. 7a, a periodic pattern with an inclined band shape and conspicuous strain concentrations can be observed in the strain fields. These strain concentrations occurred at the intersection zones between adjacent longitudinal and transverse fiber bundles. These zones resulted in the crimping and interlocking of bundles, thus leading to strength degradation of the bundles and a complex stress state. When the strain concentrations reached a certain level, matrix cracking and subsequent damage to the fiber bundles appeared in these regions. The strains on the surfaces of the transverse bundles are much larger than those of the longitudinal bundles, which reveals that the longitudinal tensile modulus is much higher. The distribution of strains in the simulation generally reproduces the strain fields in the DIC analysis, with a more obvious periodic pattern because of the ideal periodic geometric model. Fig. 8 shows the evolution of the longitudinal strains ε_{yy} with increasing load at 900 °C and the corresponding simulation results. The strain fields show a similar pattern to that at room temperature. However, more severe strain concentrations can be observed at 900 °C, indicating that the material is more prone to cracking. This is related to the weakening of the longitudinal bundles at high temperature, which contribute to preventing the formation and propagation of “intersection-zone” damage in the composites.

In order to further study the strain distribution of the 2D woven $\text{SiO}_2/\text{SiO}_2$ composites, the profiles of local strains measured by DIC at room temperature are shown in Fig. 9 for two woven RVEs. Fig. 9b and c shows the transverse and longitudinal strain distributions along the red line in Fig. 9a. These profiles confirm the previous descriptions, that is,

the strain distribution exhibits obvious periodicity between the two RVEs, which are divided by the white dotted line in Fig. 9a. In each RVE, the values of the strains vary with the woven structure and the amplitudes of the strains increase with the applied load. Moreover, as the load increases, the nonhomogeneity of the strain distributions becomes more notable, such as the three peaks of the ε_{yy} profile in the region of 1200–1600 pixels. The surface of the tested specimen was observed by scanning electron microscopy (SEM) after fracture. The SEM images of the yellow rectangular region in Fig. 9a are shown in Fig. 9d and e. Cracks appear at the SiO_2 matrix between adjacent fiber bundles, which account for the sudden increase in strain under relatively high loads. Similarly, the profiles of local strains at 900 °C are shown in Fig. 10. Figs. 10b and c present the transverse and longitudinal strain distributions along the red line in Fig. 10a. The SEM image of the yellow rectangular region in Fig. 10a is shown in Fig. 10d. It can be seen from Fig. 10d that in addition to the cracks at the matrix between adjacent fiber bundles, the matrix on the surfaces of the fiber bundles is also cracked.

4.3. Damage evolution and final failure

Figs. 11 and 12 present the simulated damage evolution, including damage to both the matrix and the fiber bundles, with increasing load at room temperature and 900 °C, respectively. As can be seen from Figs. 11 and 12, damage began at the edges of the composites both at room temperature and 900 °C, which is related to the initial defects during the preparation process. As the load increased, the damage at the edges propagated to the interior of the composites. More specifically, the

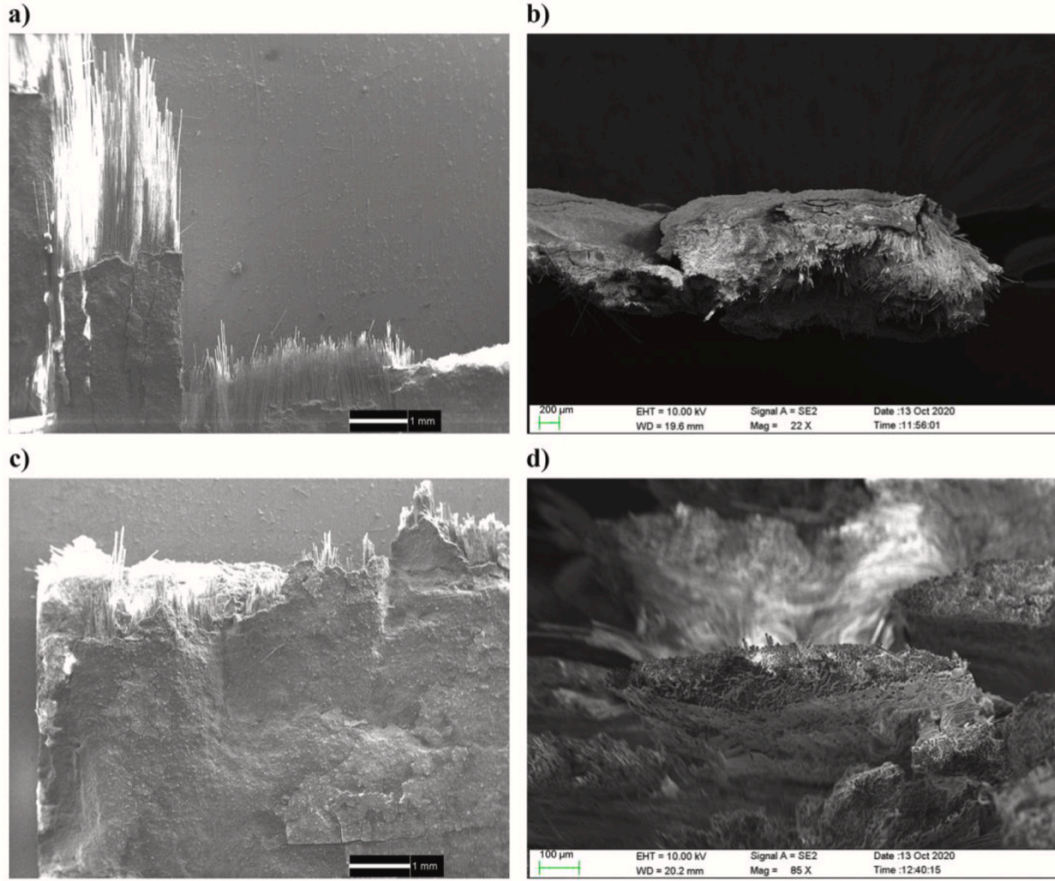


Fig. 17. The SEM images of the fracture surfaces of the composites at a), b) room temperature and c), d) 900 °C.

damage expanded through the matrix between adjacent longitudinal and transverse fiber bundles, and subsequently affected the longitudinal and transverse bundles on one cross-section. The bundles cross and crimp in such areas, which are regarded as critical regions. At room temperature, nonlinearity of the stress–strain curve occurs earlier and is more obvious at room temperature. In contrast, at 900 °C, nonlinearity appears only after the fiber bundles are damaged. When the load is close to the maximum value, the matrix damage tends to be saturated. At this time the composite still retains load-bearing capacity, indicating that the main load-bearing constituent is the fiber bundles, which dominate the final failure.

Figs. 13 and 14 show the conditions of final failure captured during the experiments and simulated in the PFA at various temperatures. It can be observed from Figs. 13a and 14a that the composites were fractured at the longitudinal fiber bundles, and the fracture surfaces were generally parallel to the inclined bands both at room temperature and 900 °C. In Figs. 13b and 14b, the matrix damage, longitudinal damage of fiber bundles and transverse damage of fiber bundles are shown respectively from left to right. The damaged zones match well with the intersection zones mentioned above. These intersection zones are considered critical regions in such twill woven composites, which experience the initiation and development of damage. This further leads to the degradation of the stiffness and strength of the composites. In Fig. 13a, fiber breakage and pull-out on the left edge can be observed. When the stress exceeded the maximum value, the composite did not fracture throughout the cross section; the fracture surface exhibited jagged features. The above phenomena demonstrate the non-brittle fracture of the composite at room temperature, which results from the crack-deflection function of the interface and the mass of pull-out of the quartz fibers. Nevertheless, the failure of the composite presents brittle characteristics at 900 °C, which

is related to the embrittlement of the interface and the quartz fibers. The composite fractured rapidly throughout the cross-section after the peak stress. The fracture surface at 900 °C is flatter than that at room temperature. The ε_{yy} evolution and damage development of individual points near the locations of final failure were extracted from the DIC results and simulation results respectively. Fig. 15a and Fig. 16a present the above information from the matrix region at various temperatures. The data from the fiber bundle regions are shown in Figs. 15b and 16b respectively. In Figs. 15 and 16, the DIC results are presented in the form of lines, and the simulation results are presented as lines and scatters. A sharp increase in strains before final failure can be observed in these figures, indicating the rapid propagation of cracks at this time. Unlike the synchronous increase of strains and damage variable values in Fig. 16a, the strain level in Fig. 15a remains relatively stable. This phenomenon results from the more severe propagation of matrix cracks at 900 °C. Additionally, the data confirm that the strain level of the matrix is much higher than that of the fiber bundles. To display the fracture morphology more explicitly, the SEM images of the fracture surfaces of the composites at room temperature and 900 °C are shown in Fig. 17.

5. Conclusion

In this study, the tensile behaviors of a 2D twill woven $\text{SiO}_2/\text{SiO}_2$ composite at room temperature and 900 °C were investigated thoroughly by experiments and simulations. Simulations of the mechanical properties, strain distributions and damage behaviors show good consistency with the experimental results. Based on the above results and discussions, several significant conclusions can be drawn:

- (1) The distributions of strains exhibit obvious periodic patterns, which are strongly related to the woven structures of the composites. As the load increases, the nonhomogeneity of the strain distributions becomes more notable. In addition, band-shaped strain concentrations can be observed at the intersection zones between adjacent longitudinal and transverse fiber bundles. These intersection zones are regarded as critical regions of 2D twill woven SiO_{2f}/SiO₂ composites under tensile loading.
- (2) The elastic modulus (4.05 GPa) and ultimate strength (22.04 MPa) at 900 °C were lower than those (4.36 GPa and 36.16 MPa, respectively) at room temperature, which is due to the degradation of the material properties of different constituents. At room temperature, the stress-strain curve exhibited notable nonlinearity in the early stage, and the crack deflection of the interface and conspicuous fiber pull-out resulted in the non-brittle fracture of the composite. Inversely, the stress-strain curve remained linear at 900 °C until fiber breakage occurred, and its final failure exhibited brittle features.
- (3) The macroscopic mechanical properties obtained in the experiments and the local information provided by the DIC results collectively verify the validity of the PFA model in this study. Additionally, detailed damage evolution and the conditions of final failures were found via the finite-element simulations. This PFA model can evaluate the mechanical behaviors of composites rapidly and accurately, thus contributing to composite design and optimization.

Declaration of competing interest

The authors declare that they have no known competing financial interests or personal relationships that could have appeared to influence the work reported in this paper.

Acknowledgements

This work was supported by the National Natural Science Foundation of China [grant numbers 51772009 and 51911530201].

References

- [1] N.P. Bansal, J. Lamon, *Ceramic Matrix Composites: Materials, Modeling and Technology*, John Wiley & Sons, 2014.
- [2] B. Li, C.R. Zhang, F. Cao, S.Q. Wang, Y. Bin Cao, G.J. Qi, Y.G. Jiang, Effect of pyrolysis temperature on the properties of three-dimensional silica fiber reinforced nitride matrix composites, *J. Mater. Eng. Perform.* 17 (1) (2008) 111–114, <https://doi.org/10.1007/s11665-007-9146-8>.
- [3] C. Li, Z. Chen, J. Zhu, Y. Liu, Y. Jiang, T. Guan, B. Li, L. Lin, Mechanical properties and microstructure of 3D orthogonal quartz fiber reinforced silica composites fabricated by silicasol-infiltration-sintering, *Mater. Des.* 36 (2012) 289–295, <https://doi.org/10.1016/j.matdes.2011.11.022>.
- [4] C.M. Xu, S.W. Wang, X.X. Huang, J.K. Guo, Processing and properties of unidirectional SiO_{2f}/SiO₂ composites, *Ceram. Int.* 33 (4) (2007) 669–673, <https://doi.org/10.1016/j.ceramint.2005.12.017>.
- [5] Y. Song, *Preparation and Properties for Broadband Wave-Transparent Two Dimensional Silica Fiber Reinforced Ceramic Matrix Composites* [Master thesis], National University of Defense Technology, China, 2010.
- [6] Y. Liu, J. Zhu, Z. Chen, Y. Jiang, Mechanical behavior of 2.5D (shallow straight-joint) and 3D four-directional braided SiO_{2f}/SiO₂ composites, *Ceram. Int.* 38 (5) (2012) 4245–4251, <https://doi.org/10.1016/j.ceramint.2012.01.083>.
- [7] Y. Xiang, F. Cao, J. Cao, X. Chen, Q. Xiong, Effects of high-temperature annealing on microstructure and mechanical property of SiO_{2f}/SiO₂ composites, *Vacuum* 144 (2017) 1–7, <https://doi.org/10.1016/j.vacuum.2017.07.005>.
- [8] C. Chen, *Characterization of New Silica Fibers, Preparation and Properties of New Silica Fibers Reinforced Silica Matrix Composites* [Master thesis], National University of Defense Technology, China, 2014.
- [9] Y. Liu, *Influence of Quartz Fabric Structures on the Mechanical Properties of Silica Matrix Composites* [PhD thesis], Nanjing University of Aeronautics and Astronautics, China, 2013.
- [10] Y. Liu, Z. Chen, J. Zhu, Y. Jiang, B. Li, F. Cao, Mechanical properties of unidirectional and five-directional braided SiO_{2f}/SiO₂ composites, *J. Appl. Mech. Trans. ASME* 47 (1980) 329–334, <https://doi.org/10.1115/1.3153664>.
- [11] D. Xu, *Processing and Properties of Three Dimensional SiO_{2f}/SiO₂ Composite by Sol-Gel Method* [Master thesis], Harbin Institute of Technology, China, 2017.
- [12] Y. Xiang, Q. Wang, Z. Peng, F. Cao, High-temperature properties of 2.5D SiO_{2f}/SiO₂ composites by sol-gel, *Ceram. Int.* 42 (11) (2016) 12802–12806, <https://doi.org/10.1016/j.ceramint.2016.07.017>.
- [13] Y. Gao, L. Zhang, J. Chen, X. Wang, H. Cheng, Preparation and properties of an oxide fiber-reinforced silica matrix composite, 2017, pp. 1041–1048, <https://doi.org/10.1111/ijac.12696>.
- [14] Y. Zheng, S. Wang, Effect of moderately high temperature heat treatment on surface morphology and structure of quartz fibers, *Appl. Surf. Sci.* 258 (10) (2012) 4698–4701, <https://doi.org/10.1016/j.apsusc.2012.01.062>.
- [15] D. Shi, Z. Cheng, Z. Li, X. Yang, M. Wang, Viscoplastic constitutive model for Ni-based directionally solidified superalloy: experimental validation on notched specimen, *Eng. Fail. Anal.* 118 (2020), 104930, <https://doi.org/10.1016/j.engfailanal.2020.104930>.
- [16] V.P. Rajan, M.N. Rossol, F.W. Zok, Optimization of digital image correlation for high-resolution strain mapping of ceramic composites, *Exp. Mech.* 52 (9) (2012) 1407–1421, <https://doi.org/10.1007/s11340-012-9617-1>.
- [17] F. Bernachy-Barbe, L. Gélébart, M. Bornert, J. Crépin, C. Sauder, Characterization of SiC/SiC composites damage mechanisms using Digital Image Correlation at the tow scale, *Compos. Appl. Sci. Manuf.* 68 (2015) 101–109, <https://doi.org/10.1016/j.compositesa.2014.09.021>.
- [18] L. Yu, B. Pan, Experimental study of tensile properties and deformation evolutions of 2D and 2.5D woven SiO_{2f}/SiO₂ composites using single-camera stereo-digital image correlation, *Compos. Struct.* 200 (2018) 589–598, <https://doi.org/10.1016/j.compstruct.2018.05.135>.
- [19] X. Teng, D. Shi, Z. Cheng, X. Jing, S. Lyu, X. Yang, Investigation on non-uniform strains of a 2.5D woven ceramic matrix composite under in-plane tensile stress, *J. Eur. Ceram. Soc.* 40 (1) (2020) 36–48, <https://doi.org/10.1016/j.jeurceramsoc.2019.08.030>.
- [20] P. Meyer, A.M. Waas, Experimental results on the elevated temperature tensile response of SiC/SiC ceramic matrix notched composites, *Compos. B Eng.* 143 (2018) 269–281, <https://doi.org/10.1016/j.compositesb.2018.01.019>.
- [21] D. Zhang, P. Meyer, A.M. Waas, An experimentally validated computational model for progressive damage analysis of notched oxide/oxide woven ceramic matrix composites, *Compos. Struct.* 161 (2017) 264–274, <https://doi.org/10.1016/j.compstruct.2016.11.001>.
- [22] S.V. Lomov, D.S. Ivanov, I. Verpoest, M. Zako, T. Kurashiki, H. Nakai, S. Hirose, Meso-FE modelling of textile composites: road map, data flow and algorithms, *Compos. Sci. Technol.* 67 (9) (2007) 1870–1891, <https://doi.org/10.1016/j.compscitech.2006.10.017>.
- [23] X. Jing, Z. Cheng, X. Teng, X. Yang, D. Shi, Reconstruction of meso-structure and numerical simulations of the mechanical behavior of three-dimensional four-directional braided ceramic matrix composites, *Ceram. Int.* 46 (18) (2020) 29309–29320, <https://doi.org/10.1016/j.ceramint.2020.08.107>.
- [24] H. Lin, L.P. Brown, A.C. Long, Modelling and simulating textile structures using TexGen, *Adv. Mater. Res.* 331 (2011) 44–47, <https://doi.org/10.4028/www.scientific.net/AMR.331.44>.
- [25] I. Verpoest, S.V. Lomov, Virtual textile composites software WiseTex: integration with micro-mechanical, permeability and structural analysis, *Compos. Sci. Technol.* 65 (15–16) (2005) 2563–2574, <https://doi.org/10.1016/j.compscitech.2005.05.031>.
- [26] S.P. Ng, P.C. Tse, K.J. Lau, Numerical and experimental determination of in-plane elastic properties of 2/2 twill weave fabric composites, *Compos. B Eng.* 29 (6) (1998) 735–744, [https://doi.org/10.1016/S1359-8368\(98\)00025-0](https://doi.org/10.1016/S1359-8368(98)00025-0).
- [27] C. Wang, A. Roy, V.V. Silberschmidt, Z. Chen, Modelling of damage evolution in braided composites: recent developments, *Mech. Adv. Mater. Mod. Process.* 3 (1) (2017), 15, <https://doi.org/10.1186/s40759-017-0030-4>.
- [28] I. Lapczyk, J.A. Hurtado, Progressive damage modeling in fiber-reinforced materials, *Compos. Appl. Sci. Manuf.* 38 (11) (2007) 2333–2341, <https://doi.org/10.1016/j.compositesa.2007.01.017>.
- [29] M. Wang, P. Zhang, Q. Fei, F. Guo, Modified micro-mechanics based multiscale model for progressive failure prediction of 2D twill woven composites, *Chin. J. Aeronaut.* 33 (7) (2020) 2070–2087, <https://doi.org/10.1016/j.cja.2019.10.009>.
- [30] D. Shi, X. Teng, X. Jing, S. Lyu, X. Yang, A multi-scale stochastic model for damage analysis and performance dispersion study of a 2.5D fiber-reinforced ceramic matrix composites, *Compos. Struct.* 248 (2020), 112549, <https://doi.org/10.1016/j.compstruct.2020.112549>.
- [31] P. Maimí, P.P. Camanho, J.A. Mayugo, C.G. Dávila, A continuum damage model for composite laminates: Part II - computational implementation and validation, *Mech. Mater.* 39 (10) (2007) 909–919, <https://doi.org/10.1016/j.mechmat.2007.03.006>.
- [32] Y. Xiang, Q. Wang, F. Cao, Y. Ma, D. Quan, Sol-gel process and high-temperature property of SiO₂/ZrO₂-SiO₂ composites, *Ceram. Int.* 43 (1) (2017) 854–859, <https://doi.org/10.1016/j.ceramint.2016.10.020>.
- [33] C. Zhu, F. Cao, Y. Xiang, Z. Peng, Thermal shock resistance of Al₂O₃/SiO₂ composites by sol-gel, *Ceram. Int.* 45 (9) (2019) 11270–11274, <https://doi.org/10.1016/j.ceramint.2019.02.201>.
- [34] Y. Zhu [PhD thesis]. Research on Prediction of Damage Failure and Fatigue Life for C/C Composites, Nanjing University of Aeronautics and Astronautics, China, 2012.
- [35] Z. Hashin, Failure criteria for unidirectional fiber composites, *J. Appl. Mech. Trans. ASME* 47 (1980) 329–334, <https://doi.org/10.1115/1.3153664>.